INTERFACE

royalsocietypublishing.org/journal/rsif

Research

Cite this article: Rix J, Uckermann O, Kirsche K, Schackert G, Koch E, Kirsch M, Galli R. 2022 Correlation of biomechanics and cancer cell phenotype by combined Brillouin and Raman spectroscopy of U87-MG glioblastoma cells. *J. R. Soc. Interface* **19**: 20220209. https://doi.org/10.1098/rsif.2022.0209

Received: 15 March 2022
Accepted: 20 June 2022

Subject Category:
Life Sciences–Physics interface

Subject Areas:
biomechanics, biophysics, medical physics

Keywords:
Brillouin, Raman, spheroids, glioblastoma

Author for correspondence:
Roberta Galli
e-mail: roberta.galli@tu-dresden.de

Electronic supplementary material is available online at https://doi.org/10.6084/m9.figshare.c.6069977.

THE ROYAL SOCIETY PUBLISHING

Correlation of biomechanics and cancer cell phenotype by combined Brillouin and Raman spectroscopy of U87-MG glioblastoma cells

Jan Rix[1], Ortrud Uckermann[2,3], Katrin Kirsche[2], Gabriele Schackert[2], Edmund Koch[1], Matthias Kirsch[2,5,6] and Roberta Galli[4]

[1]Clinical Sensoring and Monitoring, Department of Anesthesiology and Intensive Care Medicine, Faculty of Medicine Carl Gustav Carus,[2]Neurosurgery, Faculty of Medicine Carl Gustav Carus,[3]Division of Medical Biology, Department of Psychiatry, Faculty of Medicine and University Hospital Carl Gustav Carus, and [4]Department of Medical Physics and Biomedical Engineering, Faculty of Medicine Carl Gustav Carus, TU Dresden, Fetscherstrasse 74, D-01307 Dresden, Germany
[5]Klinik für Neurochirurgie, Asklepios Kliniken Schildautal, Karl-Herold-Strasse 1, D-38723 Seesen, Germany
[6]National Center for Tumor Diseases (NCT), Partner Site Dresden, Fetscherstrasse 74, D-01307 Dresden, Germany

JR, 0000-0001-5283-0290; EK, 0000-0003-0554-2178

The elucidation of biomechanics furthers our understanding of brain tumour biology. Brillouin spectroscopy is a new optical method that addresses viscoelastic properties down to subcellular resolution in a contact-free manner. Moreover, it can be combined with Raman spectroscopy to obtain co-localized biochemical information. Here, we applied co-registered Brillouin and Raman spectroscopy to U87-MG human glioblastoma cells *in vitro*. Using two-dimensional and three-dimensional cultures, we related biomechanical properties to local biochemical composition at the subcellular level, as well as the cell phenotype. Brillouin and Raman mapping of adherent cells showed that the nucleus and nucleoli are stiffer than the perinuclear region and the cytoplasm. The biomechanics of the cell cytoplasm is affected by culturing conditions, i.e. cells grown as spheroids are stiffer than adherent cells. Inside the spheroids, the presence of lipid droplets as assessed by Raman spectroscopy revealed higher Brillouin shifts that are not related to a local increase in stiffness, but are due to a higher refractive index combined with a lower mass density. This highlights the importance of locally defined biochemical reference data for a correct interpretation of the Brillouin shift of cells and tissues in future studies investigating the biomechanics of brain tumour models by Brillouin spectroscopy.

1. Introduction

The importance of biomechanics for tumour biology is increasingly acknowledged [1]. Tumours generally exhibit biochemical and biomechanical properties that differ from those of normal tissue. In addition, the metastatic potential of tumour cells is linked to the cell's mechanical properties [2]. Softer cell nuclei are related to a higher metastatic spread [3]. Moreover, recent research suggests that mechanical stress and increased activation of mechanosignalling promote malignant transformation and metastatic processes [4]. They also affect tissue perfusion, as well as angiogenesis [1]. A comprehensive analysis of biomechanics provides important insights into disease-induced changes in stiffness [5]. Therefore, strategies that consider tumour mechanics might lead to effective therapeutic approaches of treatment-resistant or metastatic cancer [6].

In neuro-oncology, the study of cell biomechanics is still in its infancy, with some research attributing tremendous importance to it. Atomic force microscopy (AFM) allowed World Health Organization (WHO) grade II, III and IV astrocytomas to be discriminated in terms of the different degrees of malignancy [7]. In

experimental gliomas and brain metastases, magnetic resonance elastography demonstrated decreased viscosity and elasticity compared with brain parenchyma. In this regard, brain metastases with an infiltrative growth pattern were softer than solid glioma [8]. Furthermore, a correlation between the strength of the extracellular matrix and the aggressiveness of brain tumours was established based on a change in mechanosignalling [9] and durotactic stimuli were identified as a major factor for glioma cell migration [10]. Structure, motility and the proliferation of glioma cells are influenced by the biomechanical properties of the tissue [11]. However, there appears to be high interpatient variability with respect to responses to biomechanical stimuli, as shown in experiments with primary glioblastoma cell lines [12]. Systematic studies addressing the cellular and subcellular biomechanical properties of brain tumour cells are lacking so far.

The mechanics of cells can be determined by various methods; however, AFM is currently the most commonly used in tumour research [13]. Several studies performed with AFM show that cancer cells can be distinguished from normal tissue, as well as original and metastatic cancer cells, by analysing their mechanical properties. Metastatic carcinoma cells were identified by mechanical studies using AFM [14,15]. Furthermore, several authors reported tumour cells being generally softer than normal cells [16–18]. However, all studies with AFM have an inherent problem arising from the contact between the measuring instrument and the sample: since AFM probes the surface of the sample, only information about the biomechanics of the cell as a whole is obtained.

As an alternative optical contact-free technique, Brillouin spectroscopy exploits the inelastic scattering of photons of a laser beam upon interaction with gigahertz-frequency acoustic phonons in the sample. This technique is used to determine the elastic properties of materials by probing the frequency of the Brillouin shift. Brillouin spectroscopy avoids any contact with the sample while providing biomechanical information at the subcellular level [19]. The Brillouin shift describes viscoelasticity and is thus not equivalent to the analysis of rigidity (Young's modulus) that is obtained by AFM. Furthermore, the Brillouin shift depends on the local index of refraction n and mass density ρ, which are used to retrieve the longitudinal elastic modulus. Nevertheless, it has also been shown that Brillouin spectroscopy can reveal local changes in the biomechanics of cells and tissues without *a priori* knowledge of n and ρ [20,21], and that changes in the Brillouin shift correlate with changes in Young's modulus [20,22]. Therefore, the Brillouin shift is considered a proxy for the stiffness of biological materials.

Brillouin spectroscopy became available only recently for biomedical applications because previously unsolved technical challenges have been overcome. The Brillouin shift is extremely small (less than 0.001 nm), thus separating the Rayleigh scattering from the Brillouin scattering and the spectral analysis of the latter is difficult when measuring turbid materials such as biological samples. In 2016, Fiore *et al*. [23] described a relatively simple approach with a spectrograph for Brillouin spectroscopy, encompassing a multi-pass Fabry–Pérot interferometer as an ultra-narrow bandpass filter and a highly dispersive optical element obtained by combining two virtually imaged phased arrays (VIPAs). This enabled near-lossless optical isolation of the Brillouin signal that has opened the avenue to the study of biological tissue.

Recently, Brillouin microscopy was applied to three-dimensional spheroids which simulate tumours in a more realistic way than single cells by accounting for cell–cell contacts, diffusion gradients, proliferation rates and drug responses [24–26]. Studies on colorectal tumour spheroids showed that the mechanical properties were altered heterogeneously across the spheroid after drug treatment [27]. Moreover, it was shown that the osmolality of the surrounding medium affects the biomechanics of ovarian cancer cell spheroids [22]. Furthermore, the effect of micro-environmental stiffness and the degradability of hydrogels on breast cancer spheroids was demonstrated [28].

The combination of Brillouin spectroscopy and microscopic set-ups allows high-resolution mapping of biomechanical properties. Owing to tight laser beam focusing coupled with confocal detection, small spot sizes (approx. 1 µm) are achieved, enabling analysis of distinct cell compartments, e.g. cytoplasm, nucleus and nucleolus [29,30]. It should be mentioned that even smaller spot sizes are not useful as the acoustic phonon mean free path limits further resolution increase [31–33]. Furthermore, Brillouin spectroscopy can be easily combined with Raman spectroscopy for simultaneous chemo-mechanical spectroscopic analysis [34]. As Raman spectroscopy allows us to draw conclusions about the biochemical composition of a sample (i.e. lipids, proteins, nucleic acids), it may be used as a reference to correlate biochemistry and biomechanics at the very same measurement position. The benefit of a combined measurement has already been demonstrated in some studies, including single cells [34–36], human epithelial [37,38] and corneal [39] tissue as well as transgenic mouse hippocampus [40]. Besides the general feasibility of combined measurements, it was shown that the biochemical information present in the Raman spectra can be used for interpreting the Brillouin shift [41,42].

The possibility of performing Brillouin spectroscopy with near-infrared excitation in order to avoid photodamage and attain a much larger penetration depth on bulk samples was demonstrated for *in vivo* measurement by Schlüßler *et al*. in 2018 [43]. These authors performed Brillouin spectroscopy of the spinal cord of living zebrafish larvae by using a VIPA-based spectrometer and excitation at 780 nm. However, combined systems exploiting near-infrared excitation have so far found only limited application. Also VIPA-based spectrometers are rarely used in combined systems, where predominantly Fabry–Pérot-based spectrometers were used in combination with a 532 nm excitation wavelength [34,40,44]. However, the sequential spectrum acquisition of Fabry–Pérot-based spectrometers has long acquisition times owing to scanning through the frequencies [45].

Here, we addressed the relationship between the Brillouin spectrum and the cellular components in brain tumour models *in vitro* by using a combined Brillouin and Raman confocal microscopic system with near-infrared laser excitation to avoid any photodamage. The aim of this study is the correlation of biomechanics with cancer cell phenotype and the biochemical properties of glioma cells cultured under different conditions. Therefore, we addressed adherent and spheroid cell culture preparations of U87-MG glioblastoma cells. First, we used Raman spectroscopy to identify the cell compartments and used this information to determine the Brillouin shift of each compartment, showing that these have different viscoelastic properties. Then, we addressed the comparison between adherent (two dimensions) and spheroid (three dimensions) cultures of U87-MG glioblastoma cells, showing that the Brillouin shift of spheroid cells is globally higher than that of adherent cells.

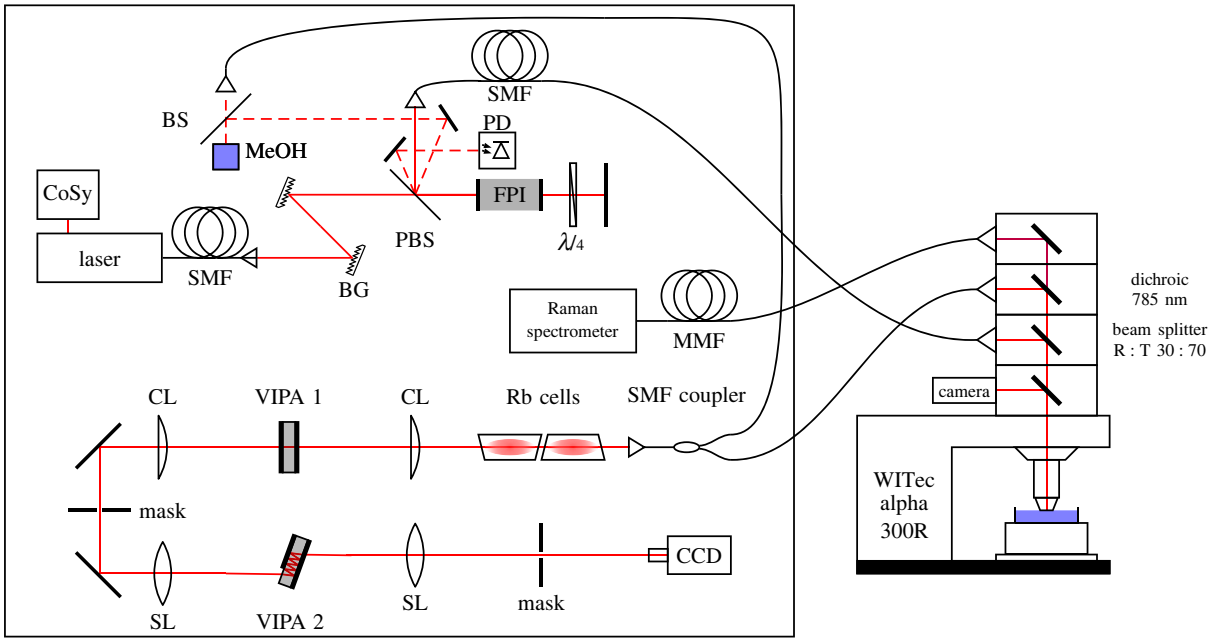

Figure 1. Experimental set-up of the combined Brillouin and Raman system consisting of a 780.24 nm laser, a compact saturation spectroscopy module (CoSy), single/multi-mode fibres (SMF/MMF), Bragg gratings (BG), a polarizing beam splitter (PBS), a Fabry–Pérot interferometer (FPI), a photodiode (PD), neutral beam splitter (BS), cylindrical/spherical lenses (CL/SL) and virtually imaged phased arrays (VIPAs).

Furthermore, the combination of Raman and Brillouin spectroscopy highlighted biochemical cues, underlining the local variation of the Brillouin shift observed within the spheroids.

2. Material and methods

2.1. Cell culture and sample preparation

For adherent cultivation (two-dimensional cell preparations), 20 000–50 000 human U87-MG cells were seeded on Raman-grade CaF_2 slides and cultured for 2–3 days in Dulbecco's modified Eagle medium (DMEM; Thermo Fisher Scientific Inc., Waltham, MA) at 37°C and 5% CO_2. For Raman–Brillouin mappings, slides were transferred to a dish and completely covered with fresh DMEM. For reference measurements, adherent cells grown on CaF_2 slides were fixed with 4% formalin for 30 min and washed with distilled water twice.

For three-dimensional spheroid cultivation, U87-MG tumour cells were suspended in a cell culture flask and cultured with abundant DMEM for one week. The upright positioning of the culture flask prevented the suspended cells from adhering to the walls, which initially led to the formation of cell clusters in the culture medium, which later grew to spheroids. It should be mentioned that no special scaffold was used to enforce any spheroid formation. No hydrogel or scaffold was used but spheroids were cultured free floating in DMEM. Culture flasks were gently shaken to resuspend the spheroids every 2–3 days. For the measurement, a few spheroids were transferred to a CaF_2 slide and covered with DMEM.

For multiphoton microscopy, spheroids were collected, embedded in cryotome matrix (OCT; CellPath Ltd, Newtown, UK) and frozen at −80°C. Cryosections of 10 µm were prepared on glass slides, whereby the fifth section through a spheroid was stored at −20°C until use. Coherent anti-Stokes Raman scattering (CARS) imaging of whole spheroids proved homogeneity between the internal and external regions, which is in line with previous findings [46].

2.2. Combined Brillouin and Raman spectroscopic system

The layout of the combined Brillouin and Raman system is shown in figure 1. A tunable diode laser (TApro; TOPTICA Photonics AG, Gräfelfing, Germany) was used as the photon source. Stabilization to the ^{85}Rb $F_g = 3$ transition at $\lambda = 780.24$ nm ensured high wavelength accuracy by using Doppler-free saturation spectroscopy (CoSy; TOPTICA Photonics AG, Gräfelfing, Germany). Two Bragg gratings (NoiseBlock; ONDAX Inc., Monrovia, CA) were used to filter out the amplified spontaneous emission (ASE) in order to suppress the background. A doubly passed Fabry–Pérot interferometer (tunable Fabry–Pérot–Etalon free spectral range (FSR) = 15 GHz; LightMachinery Inc., Nepean, Canada) further suppressed the ASE to ensure the highest signal-to-noise ratio. In this process, a $\lambda/4$-wave plate rotated the light polarization direction so that the light was reflected off the polarizing beam splitter on the return path. One of the ghost beams appearing at the polarizing beam splitter was used to stabilize the Fabry–Pérot interferometer to its maximum transmission by detecting the light power via a photodiode. Another ghost beam was used as the excitation light source for a reference beam path.

The excitation light was coupled in a single-mode fibre and propagated to an upright reflection microscope (WITec alpha 300R; WITec GmbH, Ulm, Germany). Inside the microscope a 30 : 70 beam splitter directed the monochromatic light to the sample, which was placed on an *xyz* stage. The laser power on the sample was 20 mW. A Zeiss N-Achroplan 40×/0.75NA water-dipping objective was used for adherent cell and spheroid measurements in medium and a Zeiss Epiplan-Neofluar 50×/0.8NA objective for fixed samples.

The backscattered light was separated by wavelength using a dichroic mirror. Light with a wavelength above 785 nm (Raman scattered light) was passed to a commercial Raman spectrometer (UHTS 400; WITec GmbH, Ulm, Germany) whereas light with a wavelength below 785 nm (Brillouin and Rayleigh scattered light) was passed to the Brillouin spectrometer.

In the Brillouin spectrometer, two vapour cells (Rubidium Vapor Cell TG-ABRB-Q; Precision Glassblowing Inc., Englewood, CO) were used to remove the Rayleigh scattered light, exploiting absorption on the same rubidium transition used for laser stabilization. A two-stage VIPA (LightMachinery Inc., Nepean, Canada) set-up [47] was used for the spectral analysis of Brillouin scattering. The orthogonally arranged VIPAs had a free spectral range of $FSR_1 = 15$ GHz and $FSR_2 = 21.6$ GHz, resulting in a further suppression of the ASE [48]. A CCD camera (iDUS 420A-BR-DD; Andor Technology Ltd, Belfast, UK) with

a magnification objective (InfiniProbe TS-160; Infinity Photo-Optical Company, Centennial, CO) was used to acquire the Brillouin spectra. The detector resolution was 44 MHz/pixel. The optical contrast of the spectrometer (peak-to-background ratio) amounted to 90 dB and the spectral resolution (full width at half maximum (FWHM) of the laser line) was approximately 400 MHz.

In a reference beam path, the Brillouin signal of methanol was continuously acquired in order to calibrate the spectral axis and thus precisely determine the frequency of the Brillouin band of the measured sample, compensating for thermally induced changes.

The acquisition parameters (integration times, accumulations, step sizes) are stated in the results section for the different experimental approaches.

2.3. Data analysis

After fitting the Brillouin spectrum with Lorentzian functions using custom-written Matlab software (MathWorks Inc., Natick, MA), which is based on the *lsqnonlin* function, the known Brillouin shift of methanol ($\nu_B = 3.81$ GHz [47]) was exploited in combination with the condition that the absolute frequency of the sample's Stokes and anti-Stokes signals have to be equal. The absolute shift frequency (centre), the linewidth (FWHM) and the intensity (maximum) of the Brillouin band of the sample were retrieved from the fitting procedure and used to build maps of the samples' biomechanics. Lorentzian functions were used for fitting the Brillouin bands because they approximate the damped-harmonic-oscillator characteristic of acoustic phonons. An example of the fitted Brillouin spectrum is depicted in electronic supplementary material, figure S1.

For the analysis of single-cell Brillouin shift maps, the contribution of the surrounding culture medium was removed in order to focus on the information from the cell itself. Therefore, after fitting the frequency histogram with multiple Gaussian functions (using Matlab's *lsqnonlin* function), the curve associated with the medium was subtracted, as was reported previously [49,50]. Gaussian functions were used because they take the normal distribution of the measured values into account. It should be mentioned that eliminating the contribution from the medium does not affect further analysis of the cells' mean Brillouin shift, but is rather performed to better visualize the information of interest. As examples, frequency histograms with and without the medium contribution are shown in electronic supplementary material, figure S2.

The Raman spectra were processed according to established protocols for biological samples: baseline correction followed by intensity normalization were applied (Matlab functions *msbackadj* and *msnorm*). In order to build maps of the samples' chemometrics from the Raman data, *k*-means clustering was used (*kmeans* function of Matlab with squared Euclidean distance metric).

2.4. CARS microscopy and quantification of lipid droplets

The CARS microscope is described in detail elsewhere [51]. Briefly, two pulsed erbium fibre lasers (Femto Fiber pro NIR and TNIR; TOPTICA Photonics AG, Gräfelfing, Germany) emitting at wavelengths of 781 nm and 1005 nm, respectively, were used to resonantly excite the CARS signal arising from symmetric stretching of the CH_2 groups, which are mostly contained in lipids. By scanning the lasers over the sample (laser scanning module LSM 7; Carl Zeiss AG, Jena, Germany) the CARS signal is acquired and used to build two-dimensional intensity images (2048 × 2048 pixels, 236 × 236 µm²) that enable visualization of the lipid droplets within the tissue. Fiji software [43] was used to quantify lipid droplets in CARS images. An empirical determined colour threshold of 220 was set for the 8-bit CARS signal to identify areas of high lipid concentration. Afterward, the *analyze particles* function was used to first determine the number of identified areas with a pixel size greater than 10 and then evaluate the total pixel size of these areas.

3. Results

3.1. Subcellular compartments of U87-MG glioblastoma cells identified by Raman spectroscopy show different Brillouin shifts

Combined Brillouin and Raman maps were acquired on living U87-MG adherent cells ($n = 4$, 15 s integration time and an average of two accumulations for each measurement point, 1 µm step size between adjacent points). Figure 2 shows one representative example. The results of the other specimens are shown in electronic supplementary material, figures S3.1–S3.3. In figure 2*a* the bright field image of the cell is shown and the box indicates the region mapped by spectroscopy.

First, Raman spectroscopy was exploited for identification of the mapped regions (figure 2*b*). Cluster analysis of the Raman spectra was performed, revealing the cell culture medium around the cell (grey cluster) and different cellular compartments. The centroid spectra of the three clusters associated with the cell are depicted in figure 2*c*. The blue cluster was attributed to the nucleus with its characteristic DNA bands at 785 cm^{-1}, 1341 cm^{-1} and 1579 cm^{-1} [52]. The red cluster was associated with a perinuclear region containing characteristic (phospho)lipid bands at 1264 cm^{-1} and 1308 cm^{-1} [52]. The cyan cluster was associated with the cytoplasm consisting of different protein bands (e.g. 820 cm^{-1} [52]). The assignments of the clusters to the respective cell compartments are consistent with the measurement positions as indicated in the bright field image. This assignment was also confirmed on fixed U87-MG cells ($n = 8$), which showed very similar Raman spectra in the same compartments (electronic supplementary material, figure S4).

The Brillouin shifts plotted as a heat map are shown in figure 2*d*. A region with higher Brillouin shifts is located in the centre of the cell, whereas the cell boundary is characterized by lower Brillouin shifts. By using the results of Raman cluster analysis, the Brillouin shift at the different measurement positions was assigned to the respective cell compartment (figure 2*e*). The median Brillouin shift is 5.32 GHz for the nucleus (blue cluster), 5.29 GHz for the perinuclear region (red cluster), 5.22 GHz for the cytoplasm (cyan cluster) and 5.10 GHz for the medium surrounding the cell (grey cluster). Therefore, the highest Brillouin shift was observed in the nucleus, which is consistent with the existing literature [49,50]. Moreover, it is possible to identify the nucleolus as an intracellular compartment with the highest Brillouin shift.

In figure 2*f*, single Brillouin spectra of each cluster are shown as examples. The Brillouin band shifts towards higher frequencies by moving from the medium (grey) to the nucleus (blue). Figure 2*f* also shows that the intensity of Brillouin bands decreases with higher Brillouin shifts. The Brillouin band of methanol used for calibration of the Brillouin shift frequency is visible at 3.81 GHz with constant intensity in all spectra. The Brillouin intensities map is plotted as a heat map in figure 2*g* and revealed the same morphology as the Brillouin shift. The Brillouin intensity is highest within the culturing

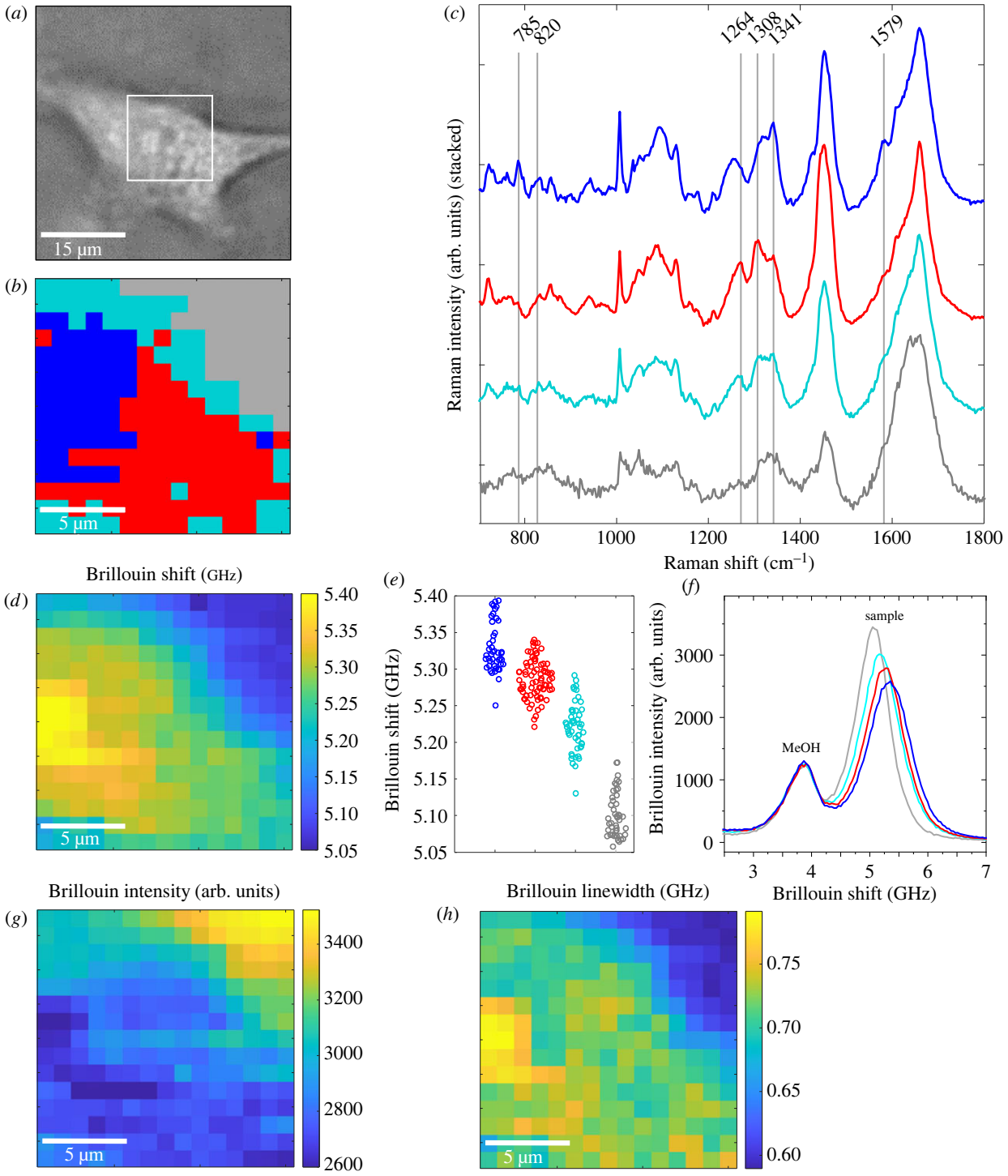

Figure 2. (*a*) Bright field image of a living U87-MG cell; white box is 15 × 15 µm^2. (*b*) Raman cluster map of this cell consisting of four different clusters. (*c*) Mean Raman spectra of the three clusters associated with the cell: the nucleus (blue), the perinuclear region (red) and the cytoplasm (cyan). (*d*) Simultaneously acquired Brillouin shift and (*g*) Brillouin intensity map revealing the cellular structure. (*e*) Brillouin shift values for each pixel are assigned to the respective cell compartment obtained by cluster analysis of Raman spectra. (*f*) Examples of Brillouin single spectra of each cluster showing the reference methanol band at 3.81 GHz and the sample's band, which shifts to higher values and decreases when going from the grey to the blue cluster. (*h*) Brillouin linewidth map revealing the high viscosity of the nucleolus.

medium and decreases inside the nucleus, being lowest in the cell nucleolus. Therefore, both these (inverse correlated [53,54]) parameters enabled mapping of the cell structure.

The width of the Brillouin band was also investigated as a proxy for the viscosity [55]. A region with highest values is located within the nucleus (figure 2*h*). In agreement with [21], this was assigned to the high viscosity of the nucleolus.

3.2. Brillouin spectroscopy reveals significantly higher Brillouin shifts for U87-MG spheroids than for U87-MG adherent cells

As acquisition of Raman spectra requires a long measurement time, thereby limiting the amount of data that can be acquired on living cells, only the Brillouin spectra were acquired in order to statistically compare the properties of

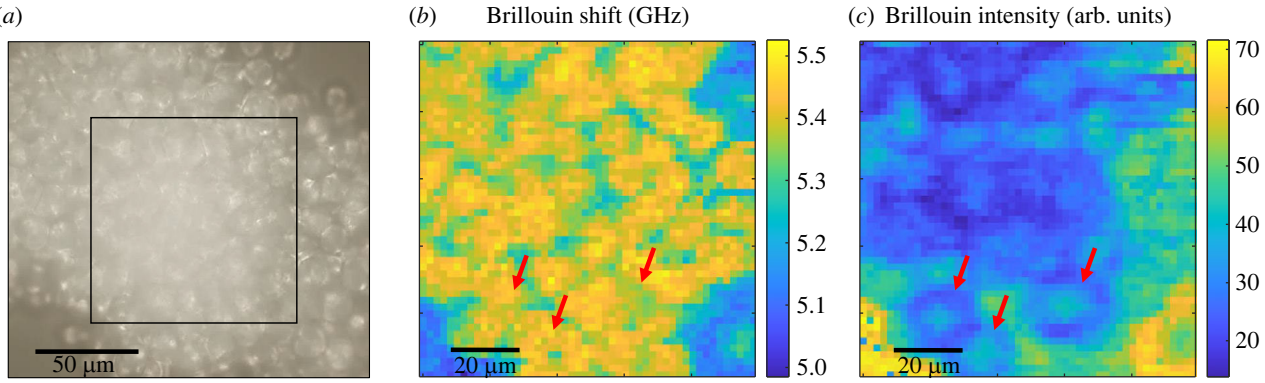

Figure 3. (*a*) Example of a bright field image of a living U87-MG spheroid, where the black box indicates the measured area. Corresponding Brillouin maps of the same spheroid using (*b*) the Brillouin shift and (*c*) the Brillouin intensity as the contrast mechanism. Red arrows indicate the positions where the structural information between the maps differs.

adherent cells and spheroids. Brillouin maps of $n = 11$ living U87-MG adherent cells and $n = 9$ living U87-MG spheroids were acquired using an integration time of 0.2 s (one accumulation for each measurement point, step size of 1 µm for adherent cells and 2 µm for cell spheroids). An example of spheroid mapping is shown in figure 3. The bright field image of the spheroid is shown in figure 3*a*. Corresponding Brillouin maps are depicted in figure 3*b*,*c* using the Brillouin shift and the Brillouin intensity as the contrast mechanism, respectively. In both maps, which are cross-sections through the spheroid, the spheroid cells can be distinguished from the surrounding culturing medium, which has lower Brillouin frequencies and higher Brillouin intensities. However, not all structures (cf. red arrows) visible in the Brillouin intensity map are observable in the Brillouin shift map and vice versa. This phenomenon might be caused by a sort of shadowing effect, because of absorption and scattering on cells lying above the measurement point, whereby the Brillouin intensity is reduced. By contrast, the Brillouin shift remains unaffected owing to confocal measurement. As the Brillouin intensity is altered according to the absorption of the above-lying cells, the Brillouin intensity map not only contains anatomical structures within the plane as reported earlier [43] but also gives information about the three-dimensional morphological structure.

In order to compare the stiffness of adherent cells and cell spheroids, the Brillouin shifts retrieved from mappings were cumulatively plotted in frequency histograms (figure 4*a*,*b*). For this purpose, all 2500 Brillouin frequency values of each adherent cell and spheroid map (probed with 1 µm and 2 µm step sizes, respectively) were collected and stored in bins of 0.1 GHz frequency width. Here, the data relating to the culturing medium were eliminated as described in the Material and methods. Gaussian fitting revealed that the main contributions to the cell and the spheroid maps are different, with one of the spheroid cells being located at a higher frequency (at about 5.4 GHz versus 5.3 GHz for adherent cells). It should be mentioned that the subcellular components (nucleus, perinuclear region and cytoplasm) were treated as one overall contribution because of their large overlap. Additionally, in both histograms, a minor contribution is visible at 5.15 GHz, which was associated with the border of the cells and is due to a combination of signals from the cell and the medium, based on the results described in the previous section (compare with figure 2*e*). Moreover, in the spheroid histogram a minor contribution at 5.34 GHz was associated with the intercellular spaces within the spheroid (compare with the Brillouin map in figure 3*b*). The statistical analysis of the main contributions of the independent measurements showed that the mean Brillouin shift of the cell spheroids is significantly higher than the mean Brillouin shift of the cells (figure 4*c*; Mann–Whitney *U*-test, $n = 9$ and 11, $p < 0.001$). The broader distribution in the case of adherent cells is due to a focusing issue, i.e. the Brillouin shift is also dependent on the axial position within a cell. This effect is minor in the case of spheroid maps because several cells with different axial positions are measured, resulting in an averaging and a smaller distribution. The frequency position of the distribution, however, is not affected by this focusing issue.

3.3. Combined Brillouin and Raman line scans of U87-MG spheroids highlight biochemical cues underlining the changes of Brillouin shift within spheroids

In order to identify the biochemical reason underlying the higher Brillouin shift that characterizes spheroids in comparison with adherent cells, combined Raman and Brillouin measurements were needed. As the acquisition of Brillouin spectra is about 100 times faster than the acquisition of useful Raman spectra, high-resolution maps—as shown in the Results—were only practicable for Brillouin spectroscopy, while for combined measurements the number of measuring points had to be reduced. Therefore, we performed combined Brillouin and Raman line scans across the living spheroids, using a 15 s integration time, four accumulations and a 1 µm step size. Two examples of 50 µm long line scans are shown in figure 5. The Brillouin shift varied in the range of approximately 5.3 GHz to approximately 5.55 GHz across the sample (figure 5*a*,*b*). A shift in the range of approximately 5.4–5.5 GHz (e.g. in line scan 1 at 9 µm and in line scan 2 at 6 µm) was attributed to the cell body and the Raman spectra were generally characterized by a similar spectral profile as found for the cells' cytoplasm. Regions where the Brillouin shift is close to approximately 5.3 GHz were interpreted as intercellular spaces (compare with figure 3*b*). The highest Brillouin shifts of approximately 5.5 GHz were observed in only a few defined positions. The comparison with Raman spectra at these positions revealed two different spectral patterns (figure 5*c*,*d*). One spectral pattern was observed in line scan 1 at 35 µm and in line scan 2 at 32 µm; here, the analysis of

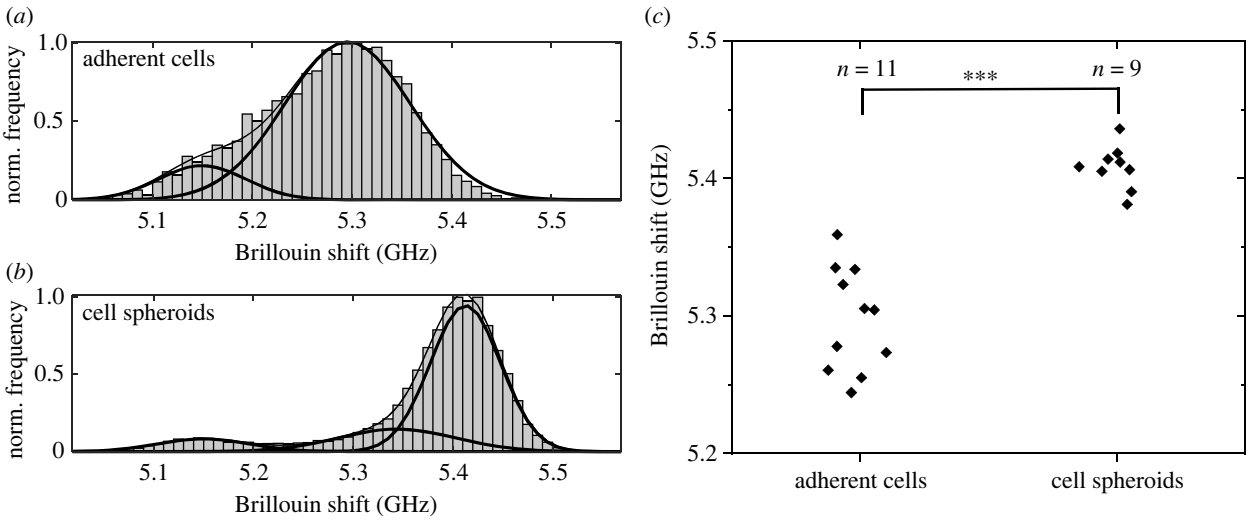

Figure 4. Cumulative frequency histograms (normalized) of the Brillouin shift values of all (*a*) living U87-MG cell ($n = 11$) and all (*b*) living U87-MG spheroid ($n = 9$) mappings, showing that there are different contributions fitted by Gaussian curves: the main contributions are at 5.3 GHz and 5.4 GHz, respectively. (*c*) Brillouin shift frequencies of the main contribution of the individual maps are significantly different (Mann–Whitney *U*-test; ***$p < 0.001$).

Raman bands (figure 5*e*,*f*) of single spectra allowed clear identification of lipids, based on the presence of strong bands at 1267 cm^{-1}, 1306 cm^{-1}, 1441 cm^{-1}, 1659 cm^{-1} and 1748 cm^{-1}. In other regions (line scan 1 at 15 µm and line scan 2 at 46 µm), the Raman spectra indicated the presence of protein-rich structures based on the bands at 863 cm^{-1}, 939 cm^{-1}, 1341 cm^{-1}, 1462 cm^{-1} and 1659 cm^{-1} [52].

In order to confirm the presence of lipid accumulation within the spheroids, CARS microscopy was used on fixed spheroids after *in vivo* spectroscopic measurement. CARS images ($n = 7$) revealed in fact the presence of intracellular lipid droplets with dimension of few micrometers (figure 6*a*), thus compatible with the results of line scans. A quantification (figure 6*b*) revealed that lipid droplets accounted for a mean average of 0.58% of the imaged area, which is compatible with the amount of measurement points characterized by a Brillouin shift close or above 5.5 GHz (compare with histogram in figure 4*b*).

4. Discussion

Brillouin spectroscopy is a rather new area in medical research and the interpretation of the Brillouin shift as a proxy for the stiffness is still a matter for investigation. By contrast, Raman spectroscopy is a successfully established technology on the verge of clinical translation.

As Raman and Brillouin scattering are simultaneously generated in the interaction of laser beams and materials, and because they can be spectrally split by a dichroic mirror, it is possible to combine the two measurements using one excitation laser, one confocal Raman microscope and two spectrometers [34,36,56]. We exploited the same principles and realized the system with an infrared laser to reduce elastic scattering and absorption by the tissue and avoid potential photodamage. In order to perform fast acquisition of Brillouin spectra with high extinction and low signal losses, we used a two-stage VIPA set-up consisting of two VIPAs with different FSRs, resulting in an increased contrast [48]. In our system, we attained very fast acquisition times for Brillouin spectra, which allowed acquisition of high-resolution maps on living cells. In addition, the Brillouin and Raman spectra were measured simultaneously so that biochemical and biomechanical data are registered to allow correlative analysis. However, Raman spectroscopy turned out to be the bottleneck for the acquisition time. This limited the acquisition of Raman spectra to relatively small maps of single cells or to line scans across spheroids.

The Raman analysis of U87-MG cells allows us to distinguish three different compartments, i.e. the cell nucleus, a perinuclear region and the cytoplasm, independently of whether the cells are fixed or living. On the other hand, Brillouin analysis on living cells in culture medium showed an increasing Brillouin shift when going from the cell boundary to the centre. By using the Raman spectral information of each pixel, a direct correlation with the Brillouin shift was possible. The three clusters attributed to the cell show higher Brillouin shifts than the surrounding culturing medium, which agrees with previous measurements [49]. The cell nucleus has a higher Brillouin shift than the cytoplasm. The nucleolus displays the highest Brillouin shift within adherent cells, and increased Brillouin bandwidth, which indicates higher viscosity. These results are fully consistent with former findings on other types of cells [30,50,57].

Comparing the Brillouin shifts of adherent cells and cell spheroids of the same cell line (U87-MG) revealed significantly higher values for the latter cells. The Brillouin shift difference of about 0.1 GHz is in line with previously reported values of single cells and spheroids of breast cancer cells (MCF-7) [28]. Line scans through spheroids showed local variations of the Brillouin shift. Brillouin shifts of about 5.5 GHz were associated with protein-rich structures and lipid droplets. Regions attributed to cytoplasm based on Raman spectra have a Brillouin shift higher than that of the cytoplasm of adherent cells.

Now, the question is which changes of Brillouin shift also indicate a change in stiffness, as the Brillouin shift ν_B depends not only on the longitudinal modulus but also on the refractive index and the mass density, as defined by the following equation:

$$\nu_B = \frac{2n}{\lambda}\sqrt{\frac{M}{\rho}}, \tag{4.1}$$

where n is the index of refraction, ρ is the mass density, M is the longitudinal modulus and λ is the excitation wavelength. Thus,

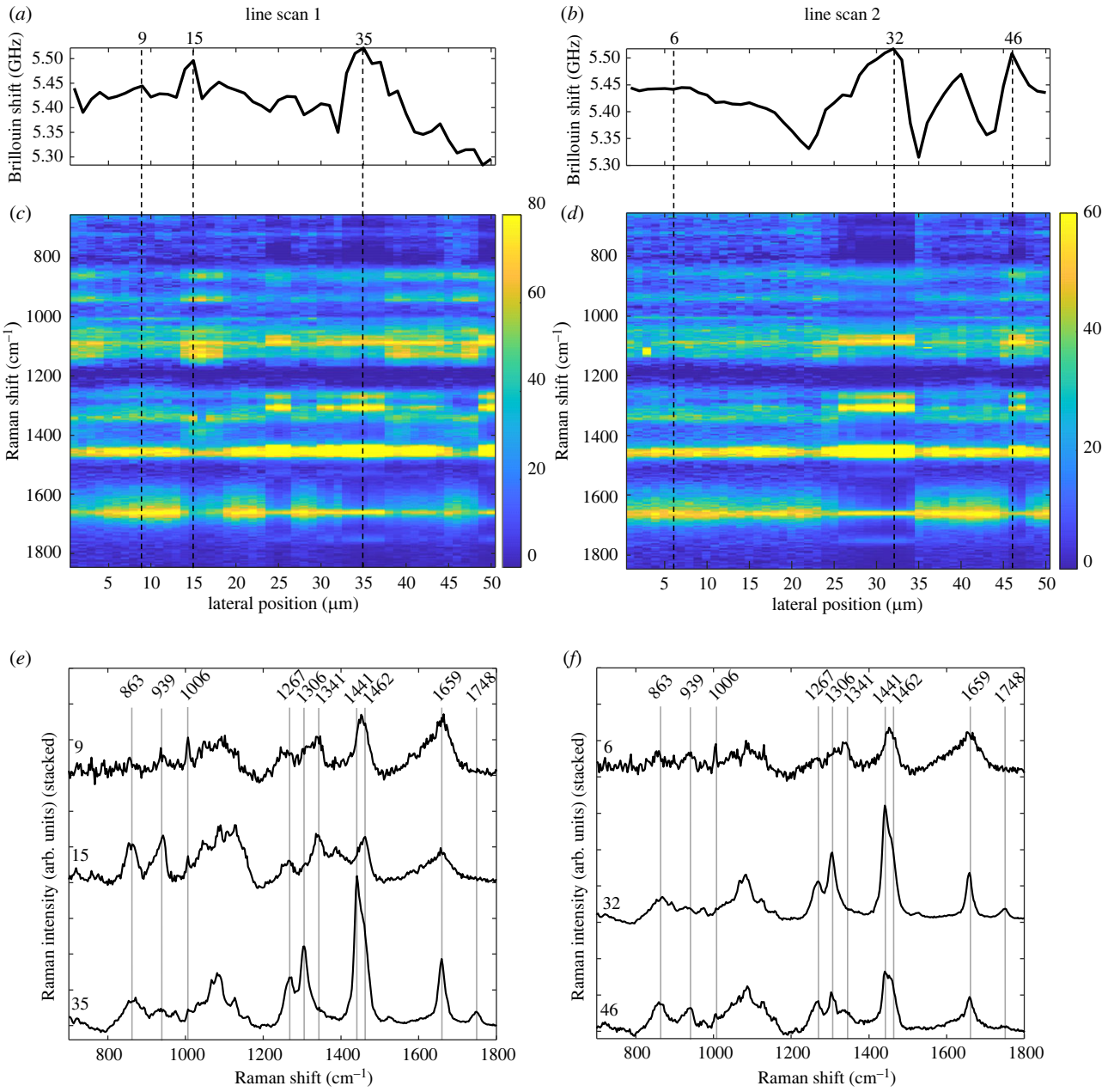

Figure 5. Results of combined line scans on living U87-MG spheroids. Brillouin shift profiles (*a*,*b*) show regions with high frequencies which can be correlated with spectral patterns visible in the Raman heat maps (*c*,*d*), in which the area-normalized Raman intensity is colour-coded. Single Raman spectra at specific positions can be attributed to cytoplasm, lipids and protein-rich structures (*e*,*f*). Note that the Raman spectrum at 46 µm in line scan 2 actually shows a linear combination of lipid and protein bands indicating the presence of both within the measuring volume.

local variations of n and ρ may lead to changes in the Brillouin shift even without any change of M.

For the cytoplasm, nucleus and nucleolus the changes of n and ρ are expected to compensate for each other according to the two-substance mixture model [21,58–60]. Therefore, the higher Brillouin shift measured in the cell nucleus and in the nucleolus of cells indicates a higher stiffness of these cellular compartments. Similarly, the higher Brillouin shifts measured in the cytoplasm of spheroid cells compared with adherent cells underline a change in biomechanical properties, i.e. a higher stiffness of spheroid cells compared with adherent cells. We attributed the difference to the culturing conditions. This finding demonstrates that the choice of brain tumour model (adherent cells versus cell spheroids) is highly relevant for the analysis of biomechanics and in agreement with other studies on breast cancer spheroids and single cells in hydrogels [28]. Future studies on other cell lines may show whether this is a general trend of tumour cells or not.

In the case of lipid droplets, the higher Brillouin shift does not indicate a stiffness higher than the surrounding cytoplasm: the mass density of lipids is lower than that of cytoplasm ($\rho = 930$ kg m^{-3} [61] versus $\rho \approx 1000$ kg m^{-3} [62]) while n is higher ($n = 1.41$ [21] versus $n = 1.375$ [63]), so that the two contributions do not compensate for each other and the ratio $n/\sqrt{\rho}$ is about 6% higher for lipids than for the cytoplasm. Indeed, the Brillouin shift of lipid droplets measured in our experiments (approx. 5.5 GHz) is approximately 5% higher than that of the cytoplasm of adherent cells (5.22 GHz). This result agrees with previous studies on adipocytes, where lipid droplets display a Brillouin shift higher than that of cytoplasm [21,64], but a 10% lower stiffness by correcting the results for the index of refraction co-registered by optical diffraction tomography [21].

The presence of lipid droplets in a glioblastoma cell culture is not surprising, as it is known that they exhibit abnormal lipid metabolism, which plays an important role

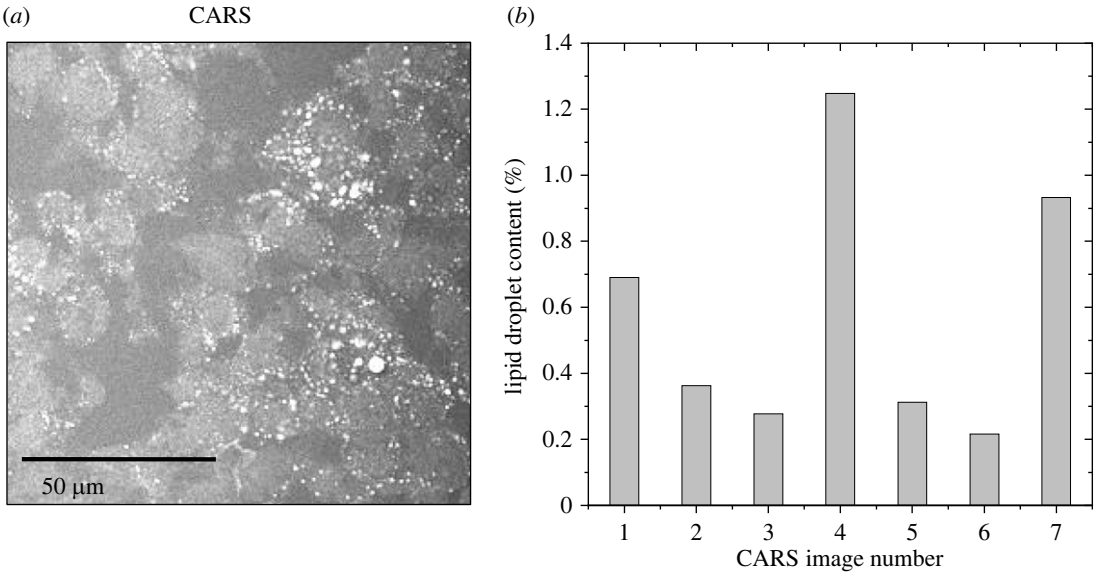

Figure 6. (*a*) Example of a CARS image of a U87-MG spheroid cryosection revealing that there are several lipid droplets within the spheroids. (*b*) Quantification of the lipid droplet content for $n = 7$ CARS images revealed values between 0.2% and 1.3%, whereby the CARS image in (*a*) corresponds to image number 1.

in aggressiveness [65,66]. Lipid droplets function as an energy reservoir for glioblastoma cells and are consumed to support survival during periods of decreased glucose levels [67]. This might explain the absence of lipid droplets in the adherent cells, which are known to express lipid droplets mainly during hypoxia, whereas the lipid droplets are absent under normoxic conditions [68,69]. Whether there are mechanisms by which cytoplasmic lipid droplets alter glioma cell biomechanics has not been investigated yet. On the other hand, lipids possess a clear spectroscopic signature in Raman spectroscopy and their presence and localization can be readily recognized with this technique, thus providing a well-suited reference tool for future investigation of the biomechanics of brain tumours.

5. Conclusion

Combined Brillouin and Raman spectroscopy proved to be a powerful tool for investigating the interplay between the biochemistry and biomechanics of glioblastoma cell cultures. The subcellular resolution of the optical system allowed for a detailed mechanical analysis of adherent cells, whereby the biochemical fingerprint from Raman spectroscopy enabled a correlation of biomechanical properties with cell compartments. The nucleus and especially the nucleolus possess different viscoelastic properties compared with the cytoplasm. Moreover, culturing conditions, which result in a different cellular architecture and appearance, have an impact on biomechanics, i.e. stiffness is significantly higher in spheroid than in adherent cells, which emphasizes the importance of choosing the appropriate tumour model in future investigations on brain tumour biomechanics. The availability of co-localized biochemical information obtained by Raman spectroscopy enabled the stiffness-related changes of the Brillouin shift to be discerned as well as the localization of stiffness changes at the subcellular level. The availability of co-registered biochemical information is very important for the correct interpretation of the biomechanical data on multicellular systems, in particular in the heterogeneous structure of a brain tumour environment. This heterogeneity may also be addressed in future studies, e.g. by investigating the microenvironment of spheroids.

Data accessibility. Datasets from this study are available without restrictions on the Open Science Framework: https://osf.io/3xn9h/?view_only=435d50723f784426bb1f4e84b1ee5459.

Authors' contributions. J.R.: data curation, formal analysis, investigation, methodology, software, visualization, writing—original draft; O.U.: conceptualization, formal analysis, methodology, supervision, validation, writing—review and editing; K.K.: data curation, investigation; G.S.: resources; E.K.: resources, supervision; M.K.: conceptualization, funding acquisition; R.G.: conceptualization, formal analysis, investigation, methodology, supervision, validation, visualization, writing—original draft, writing—review and editing.

All authors gave final approval for publication and agreed to be held accountable for the work performed therein.

Conflict of interest declaration. The authors declare no conflict of interest.

Funding. This research was partly funded by the National Center for Tumor Diseases (NCT). J.R. was funded by the Free State of Saxony (Saxon scholarship program).

References

1. Dong C, Zahir N, Konstantopoulos K. 2018 *Biomechanics in oncology*. Berlin, Germany: Springer.
2. Holenstein CN *et al.* 2019 The relationship between metastatic potential and in vitro mechanical properties of osteosarcoma cells. *MBoC* **30**, 887–898. (doi:10.1091/mbc.E18-08-0545)
3. Liu H, Wen J, Xiao Y, Liu J, Hopyan S, Radisic M, Simmons CA, Sun Y. 2014 *In situ* mechanical characterization of the cell nucleus by atomic force microscopy. *ACS Nano* **8**, 3821–3828. (doi:10.1021/nn500553z)
4. Huang S, Ingber DE. 2005 Cell tension, matrix mechanics, and cancer development. *Cancer Cell* **8**, 175–176. (doi:10.1016/j.ccr.2005.08.009)
5. Jorba I, Uriarte JJ, Campillo N, Farré R, Navajas D. 2017 Probing micromechanical properties of the extracellular matrix of soft tissues by atomic force microscopy. *J. Cell. Physiol.* **232**, 19–26. (doi:10.1002/jcp.25420)
6. Northey JJ, Przybyla L, Weaver VM. 2017 Tissue force programs cell fate and tumor aggression.

Cancer Discov. **7**, 1224–1237. (doi:10.1158/2159-8290.CD-16-0733)

7. Huml M, Silye R, Zauner G, Hutterer S, Schilcher K. 2013 Brain tumor classification using AFM in combination with data mining techniques. *BioMed Res. Int.* **2013**, e176519. (doi:10.1155/2013/176519)
8. Jamin Y *et al.* 2015 Exploring the biomechanical properties of brain malignancies and their pathologic determinants in vivo with magnetic resonance elastography. *Cancer Res.* **75**, 1216–1224. (doi:10.1158/0008-5472.CAN-14-1997)
9. Miroshnikova YA *et al.* 2016 Tissue mechanics promote IDH1-dependent HIF1α–tenascin C feedback to regulate glioblastoma aggression. *Nat. Cell Biol.* **18**, 1336–1345. (doi:10.1038/ncb3429)
10. Palamà IE *et al.* 2019 Mechanical durotactic environment enhances specific glioblastoma cell responses. *Cancers* **11**, 643. (doi:10.3390/cancers11050643)
11. Ulrich TA, de Pardo EMJ, Kumar S. 2009 The mechanical rigidity of the extracellular matrix regulates the structure, motility, and proliferation of glioma cells. *Cancer Res.* **69**, 4167–4174. (doi:10.1158/0008-5472.CAN-08-4859)
12. Grundy TJ, De Leon E, Griffin KR, Stringer BW, Day BW, Fabry B, Cooper-White J, O'Neill GM. 2016 Differential response of patient-derived primary glioblastoma cells to environmental stiffness. *Sci. Rep.* **6**, 23353. (doi:10.1038/srep23353)
13. Deng X *et al.* 2018 Application of atomic force microscopy in cancer research. *J. Nanobiotechnol.* **16**, 102. (doi:10.1186/s12951-018-0428-0)
14. Cross SE, Jin YS, Rao J, Gimzewski JK. 2007 Nanomechanical analysis of cells from cancer patients. *Nature Nanotech.* **2**, 780–783. (doi:10.1038/nnano.2007.388)
15. Xu W, Mezencev R, Kim B, Wang L, McDonald J, Sulchek T. 2012 Cell stiffness is a biomarker of the metastatic potential of ovarian cancer cells. *PLoS ONE* **7**, e46609. (doi:10.1371/journal.pone.0046609)
16. Lekka M, Laidler P, Gil D, Lekki J, Stachura Z, Hrynkiewicz AZ. 1999 Elasticity of normal and cancerous human bladder cells studied by scanning force microscopy. *Eur. Biophys. J.* **28**, 312–316. (doi:10.1007/s002490050213)
17. Li QS, Lee GYH, Ong CN, Lim CT. 2008 AFM indentation study of breast cancer cells. *Biochem. Biophys. Res. Commun.* **374**, 609–613. (doi:10.1016/j.bbrc.2008.07.078)
18. Guck J *et al.* 2005 Optical deformability as an inherent cell marker for testing malignant transformation and metastatic competence. *Biophys. J.* **88**, 3689–3698. (doi:10.1529/biophysj.104.045476)
19. Nikolić M, Conrad C, Zhang J, Scarcelli G. 2018 Noninvasive imaging: Brillouin confocal microscopy. In *Biomechanics in oncology* (eds C Dong, N Zahir, K Konstantopoulos), pp. 351–364. Advances in Experimental Medicine and Biology. Cham, Switzerland: Springer International Publishing.
20. Scarcelli G, Polacheck WJ, Nia HT, Patel K, Grodzinsky AJ, Kamm RD, Yun SH. 2015 Noncontact three-dimensional mapping of intracellular hydromechanical properties by Brillouin microscopy. *Nat. Methods.* **12**, 1132–1134. (doi:10.1038/nmeth.3616)
21. Schlüßler R *et al.* 2022 Correlative all-optical quantification of mass density and mechanics of subcellular compartments with fluorescence specificity. *Elife* **11**, e68490. (doi:10.7554/eLife.68490)
22. Conrad C, Gray KM, Stroka KM, Rizvi I, Scarcelli G. 2019 Mechanical characterization of 3D ovarian cancer nodules using Brillouin confocal microscopy. *Cel. Mol. Bioeng.* **12**, 215–226. (doi:10.1007/s12195-019-00570-7)
23. Fiore A, Zhang J, Shao P, Yun SH, Scarcelli G. 2016 High-extinction virtually imaged phased array-based Brillouin spectroscopy of turbid biological media. *Appl. Phys. Lett.* **108**, 203701. (doi:10.1063/1.4948353)
24. Duval K, Grover H, Han LH, Mou Y, Pegoraro AF, Fredberg J, Chen Z. 2017 Modeling physiological events in 2D vs. 3D cell culture. *Physiology* **32**, 266–277. (doi:10.1152/physiol.00036.2016)
25. Debnath J, Brugge JS. 2005 Modelling glandular epithelial cancers in three-dimensional cultures. *Nat. Rev. Cancer.* **5**, 675–688. (doi:10.1038/nrc1695)
26. Reynolds DS, Tevis KM, Blessing WA, Colson YL, Zaman MH, Grinstaff MW. 2017 Breast cancer spheroids reveal a differential cancer stem cell response to chemotherapeutic treatment. *Sci. Rep.* **7**, 10382. (doi:10.1038/s41598-017-10863-4)
27. Margueritat J *et al.* 2019 High-frequency mechanical properties of tumors measured by Brillouin light scattering. *Phys. Rev. Lett.* **122**, 018101. (doi:10.1103/PhysRevLett.122.018101)
28. Mahajan V, Beck T, Gregorczyk P, Ruland A, Alberti S, Guck J, Werner C, Schlüßler R, Taubenberger AV. 2021 Mapping tumor spheroid mechanics in dependence of 3D microenvironment stiffness and degradability by Brillouin microscopy. *Cancers* **13**, 5549. (doi:10.3390/cancers13215549)
29. Antonacci G, Braakman S. 2016 Biomechanics of subcellular structures by non-invasive Brillouin microscopy. *Sci. Rep.* **6**, 37217. (doi:10.1038/srep37217)
30. Elsayad K, Polakova S, Gregan J. 2019 Probing mechanical properties in biology using Brillouin microscopy. *Trends Cell Biol.* **29**, 608–611. (doi:10.1016/j.tcb.2019.04.002)
31. Caponi S, Fioretto D, Mattarelli M. 2020 On the actual spatial resolution of Brillouin Imaging. *Opt Lett.* **45**, 1063–1066.
32. Mattarelli M, Vassalli M, Caponi S. 2020 Relevant length scales in Brillouin imaging of biomaterials: the interplay between phonons propagation and light focalization. *ACS Photonics* **7**, 2319–2328. (doi:10.1021/acsphotonics.0c00801)
33. Palombo F, Fioretto D. 2019 Brillouin light scattering: applications in biomedical sciences. *Chem. Rev.* **119**, 7833–7847. (doi:10.1021/acs.chemrev.9b00019)
34. Scarponi F *et al.* 2017 High-performance versatile setup for simultaneous Brillouin-Raman micro-spectroscopy. *Phys. Rev. X* **7**, 031015. (doi:10.1103/PhysRevX.7.031015)
35. Meng Z, Lopez SCB, Meissner KE, Yakovlev VV. 2016 Subcellular measurements of mechanical and chemical properties using dual Raman-Brillouin microspectroscopy. *J. Biophotonics.* **9**, 201–207. (doi:10.1002/jbio.201500163)
36. Mattana S, Mattarelli M, Urbanelli L, Sagini K, Emiliani C, Serra MD, Fioretto D, Caponi S. 2018 Non-contact mechanical and chemical analysis of single living cells by microspectroscopic techniques. *Light Sci. Appl.* **7**, 17139. (doi:10.1038/lsa.2017.139)
37. Palombo F, Madami M, Stone N, Fioretto D. 2014 Mechanical mapping with chemical specificity by confocal Brillouin and Raman microscopy. *Analyst* **139**, 729–733. (doi:10.1039/C3AN02168H)
38. Palombo F, Madami M, Fioretto D, Nallala J, Barr H, David A, Stone N. 2016 Chemico-mechanical imaging of Barrett's oesophagus. *J. Biophotonics.* **9**, 694–700. (doi:10.1002/jbio.201600038)
39. Mercatelli R *et al.* 2019 Morpho-mechanics of human collagen superstructures revealed by all-optical correlative micro-spectroscopies. *Commun. Biol.* **2**, 1–10. (doi:10.1038/s42003-019-0357-y)
40. Palombo F, Masia F, Mattana S, Tamagnini F, Borri P, Langbein W, Fioretto D. 2018 Hyperspectral analysis applied to micro-Brillouin maps of amyloid-beta plaques in Alzheimer's disease brains. *Analyst* **143**, 6095–6102. (doi:10.1039/C8AN01291A)
41. Cardinali MA, Govoni M, Dallari D, Caponi S, Fioretto D, Morresi A. 2020 Mechano-chemistry of human femoral diaphysis revealed by correlative Brillouin–Raman microspectroscopy. *Sci. Rep.* **10**, 17341. (doi:10.1038/s41598-020-74330-3)
42. Fioretto D, Caponi S, Palombo F. 2019 Brillouin-Raman mapping of natural fibers with spectral moment analysis. *Biomed. Opt. Express.* **10**, 1469–1474. (doi:10.1364/BOE.10.001469)
43. Schlüßler R *et al.* 2018 Mechanical mapping of spinal cord growth and repair in living zebrafish larvae by Brillouin imaging. *Biophys. J.* **115**, 911–923. (doi:10.1016/j.bpj.2018.07.027)
44. Caponi S, Fioretto D, Mattarelli M. 2020 Transition across a sharp interface: data from Raman and Brillouin imaging spectroscopy. *Data Brief.* **33**, 106368. (doi:10.1016/j.dib.2020.106368)
45. Scarcelli G, Yun SH. 2008 Confocal Brillouin microscopy for three-dimensional mechanical imaging. *Nat. Photonics.* **2**, 39–43. (doi:10.1038/nphoton.2007.250)
46. Stanković T, Ranđelović T, Dragoj M, Stojković Burić S, Fernández L, Ochoa I, Pérez-García VM, Pešić M. 2021 In vitro biomimetic models for glioblastoma-a promising tool for drug response studies. *Drug Resist Updat.* **55**, 100753. (doi:10.1016/j.drup.2021.100753)
47. Berghaus KV, Yun SH, Scarcelli G. 2015 High speed sub-GHz spectrometer for Brillouin scattering analysis. *J. Visual. Exp.* **22**, e53468. (doi:10.3791/53468)
48. Berghaus K, Zhang J, Yun SH, Scarcelli G. 2015 High-finesse sub-GHz-resolution spectrometer

employing VIPA etalons of different dispersion. *Opt Lett.* **40**, 4436–4439. (doi:10.1364/OL.40.004436)

49. Zhang J, Nou A, Kim H, Scarcelli G. 2017 Brillouin flow cytometry for label-free mechanical phenotyping of the nucleus. *Lab. Chip.* **17**, 663–670. (doi:10.1039/C6LC01443G)
50. Zhang J, Alisafaei F, Nikolić M, Nou XA, Kim H, Shenoy VB, Scarcelli G. 2020 Nuclear mechanics within intact cells is regulated by cytoskeletal network and internal nanostructures. *Small* **16**, 1907688. (doi:10.1002/smll.201907688)
51. Galli R, Uckermann O, Andresen EF, Geiger KD, Koch E, Schackert G, Steiner G, Kirsch M. 2014 Intrinsic indicator of photodamage during label-free multiphoton microscopy of cells and tissues. *PLoS ONE* **9**, e110295. (doi:10.1371/journal.pone.0110295)
52. Movasaghi Z, Rehman S, Rehman DIU. 2007 Raman spectroscopy of biological tissues. *Appl. Spectrosc. Rev.* **42**, 493–541. (doi:10.1080/05704920701551530)
53. Fabelinskii IL. 1968 Theory of molecular light scattering in condensed isotropic media and gases. In *Molecular scattering of light* (ed. IL Fabelinskii), pp. 19–79. Boston, MA: Springer.
54. Still T. 2010 Basics and Brillouin light scattering. In *High frequency acoustics in colloid-based meso- and nanostructures by spontaneous Brillouin light scattering* (ed. T Still), pp. 9–34. Berlin, Germany: Springer.
55. Prevedel R, Diz-Muñoz A, Ruocco G, Antonacci G. 2019 Brillouin microscopy: an emerging tool for mechanobiology. *Nat. Methods.* **16**, 969–977. (doi:10.1038/s41592-019-0543-3)
56. Traverso AJ, Thompson JV, Steelman ZA, Meng Z, Scully MO, Yakovlev VV. 2015 Dual Raman-Brillouin microscope for chemical and mechanical characterization and imaging. *Anal. Chem.* **87**, 7519–7523. (doi:10.1021/acs.analchem.5b02104)
57. Zhang J, Scarcelli G. 2021 Mapping mechanical properties of biological materials via an add-on Brillouin module to confocal microscopes. *Nat. Protoc.* **16**, 1251–1275. (doi:10.1038/s41596-020-00457-2)
58. Barer R. 1952 Interference microscopy and mass determination. *Nature* **169**, 366–367. (doi:10.1038/169366b0)
59. Popescu G, Park Y, Lue N, Best-Popescu C, Deflores L, Dasari RR, Feld MS, Badizadegan K. 2008 Optical imaging of cell mass and growth dynamics. *Am. J. Physiol. Cell Physiol.* **295**, C538–C544. (doi:10.1152/ajpcell.00121.2008)
60. Zangle TA, Teitell MA. 2014 Live-cell mass profiling: an emerging approach in quantitative biophysics. *Nat. Methods.* **11**, 1221–1228. (doi:10.1038/nmeth.3175)
61. Bartsch TF, Longoria RA, Florin EL, Shubeita GT. 2013 Lipid droplets purified from *Drosophila* embryos as an endogenous handle for precise motor transport measurements. *Biophys. J.* **105**, 1182–1191. (doi:10.1016/j.bpj.2013.07.026)
62. Elsayad K, Werner S, Gallemí M, Kong J, Sánchez Guajardo ER, Zhang L, Jaillais Y, Greb T, Belkhadir Y. 2016 Mapping the subcellular mechanical properties of live cells in tissues with fluorescence emission–Brillouin imaging. *Sci. Signal.* **9**, rs5. (doi:10.1126/scisignal.aaf6326)
63. Choi W, Fang-Yen C, Badizadegan K, Oh S, Lue N, Dasari RR, Feld MS. 2007 Tomographic phase microscopy. *Nat. Methods.* **4**, 717–719. (doi:10.1038/nmeth1078)
64. Troyanova-Wood M, Coker Z, Traverso A, Yakovlev VV. 2017 Using Brillouin microspectroscopy to characterize adipocytes' response to lipid droplet accumulation. *Proc. SPIE* **10067**, 42–46. (doi:10.1117/12.2253391)
65. Geng F, Guo D. 2017 Lipid droplets, potential biomarker and metabolic target in glioblastoma. *Intern. Med. Rev. (Wash D C)* **3**, 10.18103/imr.v3i5.443. (doi:10.18103/imr.v3i5.443)
66. Guo D, Bell EH, Chakravarti A. 2013 Lipid metabolism emerges as a promising target for malignant glioma therapy. *CNS Oncol.* **2**, 289–299. (doi:10.2217/cns.13.20)
67. Wu X, Geng F, Cheng X, Guo Q, Zhong Y, Cloughesy TF, Yong WH, Chakravarti A, Guo D. 2020 Lipid droplets maintain energy homeostasis and glioblastoma growth via autophagic release of stored fatty acids. *iScience* **23**, 101569. (doi:10.1016/j.isci.2020.101569)
68. Bensaad K *et al.* 2014 Fatty acid uptake and lipid storage induced by HIF-1α contribute to cell growth and survival after hypoxia-reoxygenation. *Cell Rep.* **9**, 349–365. (doi:10.1016/j.celrep.2014.08.056)
69. Mesti T, Savarin P, Triba MN, Moyec LL, Ocvirk J, Banissi C, Carpentier AF. 2014 Metabolic impact of anti-angiogenic agents on U87 glioma cells. *PLoS ONE* **9**, e99198. (doi:10.1371/journal.pone.0099198)